Geotextiles and Geomembranes 44 (2016) 295–307

Contents lists available at ScienceDirect

Geotextiles and Geomembranes

journal homepage: www.elsevier.com/locate/geotexmem

A three-dimensional finite element approach for modeling biaxial geogrid with application to geogrid-reinforced soils

M.G. Hussein, M.A. Meguid*

Department of Civil Engineering and Applied Mechanics, McGill University, Montreal, Quebec, Canada

ARTICLE INFO

Article history:
Received 23 August 2015
Received in revised form
24 December 2015
Accepted 31 December 2015
Available online 28 January 2016

Keywords:
Geosynthetics
Soil-structure interaction
Biaxial geogrid
Numerical analysis
Index tests
Geogrid-reinforced soil

ABSTRACT

Understanding soil-geogrid interaction is essential for the analysis and design of geogrid-reinforced soil structures. A first step towards accurate modeling of this interaction is choosing a suitable material model for the geogrid that is capable of simulating tensile test results. The model must be able to capture the three-dimensional response of the geogrid considering its exact geometry. Modeling geogrid inclusion as a continuous sheet has proven to reasonably simulate the overall response of soil-geogrid systems; however, it does not explain the different sources of interaction between the geogrid layer and the surrounding soil. To understand the three-dimensional aspects of this complex interaction problem, a two-phase numerical investigation is developed in this study. The first phase focuses on the three-dimensional modeling of unconfined biaxial geogrid subjected to tensile loading. Applicability of the geogrid model in solving soil-structure interaction problems is then demonstrated, in the second phase, by investigating the response of a reinforced subgrade subjected to a square shaped surface loading. It is concluded that modeling the three-dimensional geogrid geometry is important to accurately capture the true response of geogrid under both confined and unconfined conditions. The modeling approach proposed in this study for the analysis of unconfined and soil-confined geogrid can be adapted for other reinforced soil applications.

1. Introduction

Geogrid reinforcement is known to be an effective method to enhance the performance and service life of different earth structures (e.g. embankments, pavements, foundations and retaining walls). Reinforced soil structures are usually designed using limit equilibrium methods. These methods do not generally provide sufficient information on the failure load and the displacements and strains developing in the reinforcement (Rowe and Mylleville, 1994; Sugimoto and Alagiyawanna, 2003). On the other hand, finite element (FE) methods have become powerful tools to efficiently predict the pre-failure displacements, and stresses generated in the reinforcement material.

Several studies that employ finite and discrete element methods to analyze geogrid-reinforced structures have been reported in the literature (Yogarajah and Yeo, 1994; Perkins and Edens, 2003; McDowell et al., 2006; Hussein and Meguid, 2013; Tran et al., 2013a,b; Mosallanezhad et al., 2016; Wang et al., 2016). Most of these studies focused on the overall response of the reinforced structure while adopting simplifying assumptions related to either the details of the geogrid geometry or the constitutive model of the geogrid material.

The nonlinear stress-strain response of geogrid polymeric material is recognized as an important characteristic that needs to be captured in both analytical and numerical modeling of reinforced-soil applications (Bathurst and Kaliakin, 2005; Kongkitkul et al., 2014; Ezzein et al., 2015). It is therefore, necessary to develop and incorporate a nonlinear constitutive model for the geogrid material to improve the accuracy of the numerical analysis. This model should contain sufficient components to characterize the unconfined response and captures the important geometric features of the geogrid before it interacts with the backfill material. In addition, the model has to be relatively simple, with respect to the number of required parameters, to facilitate implementation into existing numerical codes. A limited number of dedicated studies have been reported, to date, focusing on geosynthetic modeling in three-

* Corresponding author. Tel.: + 1 514 398 1537; fax: + 1 514 398 7361.
E-mail addresses: mahmoud.hussein3@mail.mcgill.ca (M.G. Hussein), mohamed.meguid@mcgill.ca (M.A. Meguid).

http://dx.doi.org/10.1016/j.geotexmem.2015.12.004
0266-1144/

dimensional (3D) space. Most notably, the work of Perkins and his coworkers between 2000 and 2003.

Perkins (2000, 2001) presented an elastic–plastic model for geosynthetics that accounts for the creep behavior and direction dependency of the material. The model required a total of 24 input parameters to capture the material response under axial loading. The model, treated the geogrid as a planer sheet and, therefore, did not account for the discontinuous nature of the geogrid geometry. It has been demonstrated (Perkins and Edens, 2003) that the creep components have a small effect on the calculated load–displacement response of the geosynthetic material. The results did, however, show that plasticity had a significant effect on the load–displacement relationship, particularly, as the geosynthetic material approaches failure.

Another important factor to be considered in modeling geogrid is the 3D geometry of the network structure. Modelling geogrid using planer sheet does not allow for essential features to be captured, including: i) the unique deformation characteristics of each member during unconfined tensile loading condition, and ii) the effect of bearing resistance on confined geogrid ribs.

The objective of this study is to propose a 3D modeling approach to capture the details of biaxial geogrid under both unconfined and soil-confined conditions. This is achieved in two phases as follows:

i) A 3D nonlinear FE analysis has been performed to simulate the behavior of unconfined geogrid under tensile loading. The ABAQUS-based constitutive model used in the FE analysis is capable of capturing the ranges of elastic and plastic regions of the stress–strain relationship in the short-term under monotonic tensile loading. The geogrid geometry is modeled explicitly with its detailed features including the rib and junction thicknesses and the geogrid apertures.
ii) Using the geogrid model developed in the first phase, a 3D analysis of soil-confined geogrid is then performed to examine the validity of the geogrid model. An example that involves a square footing over geogrid-reinforced soil is presented and the results are compared with experimental data.

The 3D FE models presented throughout this study have been performed using the general finite element software ABAQUS/Standard, version 6.13 (ABAQUS, 2013).

2. Modelling unconfined geogrid

The details of the experiments and the 3D FE modeling of unconfined geogrid, covered in the first phase of this study, are discussed in this section.

2.1. Tensile tests

A series of index tests involving uniaxial-tensile loading was performed to measure the load–displacement response of the biaxial geogrid samples. The geogrid properties as provided by the manufacturer are summarized in Table 1. The tests are conducted according to the ASTM standard D6637-11 (2011) on multi-rib geogrid specimens in both the machine (MD) and the cross machine (XMD) directions. The geogrid sample comprises three longitudinal ribs and six transverse bars as shown in Fig. 1. In these index tests, one of the clamps is usually fixed while the other is allowed to move and pull the geogrid specimen. A 5 kN MTS machine with constant strain rate of 10% strain/minute was used to test five identical geogrid specimens in each direction. An extensometer with a gauge length of 25 mm was mounted at the center of the specimen to measure the elongation during the test whereas the applied load was recorded using a load cell integrated into the MTS machine. It should be noted that this test procedure allows for the overall geogrid response to be measured considering homogenized characteristics of the geogrid geometry. To take into account the solid material characteristics, the load carried by each rib is obtained by dividing the applied machine load by the number of ribs in the loading direction. The directional (axial) load-strain response of the solid material is presented in Fig. 2. The mean values of the measurements obtained from the five index tests are shown with one standard deviation range bars. For both the MD and XMD, the measured values are tightly clustered around the mean which indicates that the test results in both directions are repeatable and the material properties are uniform for the tested specimens.

From Fig. 2, the geogrid response is found to be mostly nonlinear with significant plastic deformations developing as failure is approached. The maximum strength was found to be 12.8 kN/m and 20.5 kN/m for MD and XMD, respectively. These results are consistent with the values reported by the manufacturer (given in Table 1). It is noted that although the response shown in Fig. 2 represents the specific biaxial geogrid used in this study, similar approach can be used for other types of geogrid by considering the number of ribs per meter in a given direction.

2.2. Model development

Three-dimensional FE analyses are conducted to simulate the index tests considering the geometric features of the geogrid, including the different element thicknesses and the opening dimensions as per the geogrid specimen. An elastic–plastic constitutive model is used to explicitly simulate the measured nonlinear behavior of the geogrid. The numerical model is first validated with the test results and then used to investigate the detailed response of the geogrid under tensile loading. Sensitivity analyses are also performed to examine the effect of the finite element size, type, shape, and interpolation function on the calculated geogrid response. The modeling details and the findings of the sensitivity analyses are discussed below.

2.2.1. Model components

Two main components are required for the successful development of the unconfined geogrid model: i) constitutive behavior, and ii) geometry and boundary conditions. These components are discussed in this section.

Constitutive behavior: Experimental results (Fig. 2) show that the biaxial geogrid sample behaves as a nonlinear elasto-plastic

Table 1
Index properties of the biaxial geogrid.

Direction	Aperture size (mm)	Specimen size (mm)		No. of members		Ult. strength (kN/m)	Mass/unit area (g/m^2)	Stiffness @ 2% strain (kN/m)
		L	W	Long.	Trans.			
MD	29	149	78	3	6	12	215	204
XMD	37	185	58			20		292

Note: The above values are reported by the manufacturer.

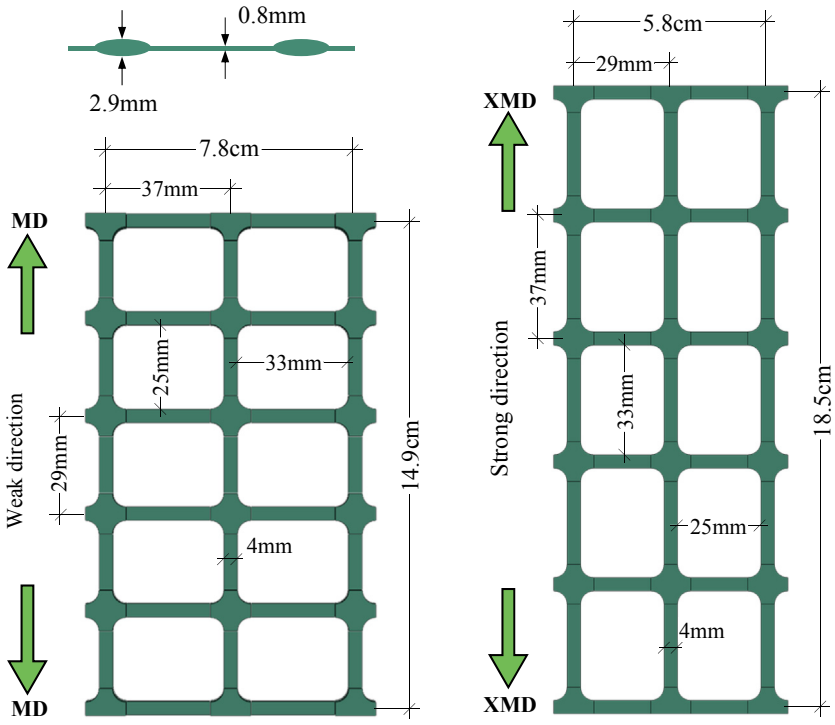

Fig. 1. Multi-rib unconfined tensile test on biaxial geogrid.

hardening material. Therefore, simplifying the response using linear elasticity (e.g. Liu et al., 2007; Abdi and Zandieh, 2014) may lead to incorrect response. A practical constitutive model that is capable of describing both the material nonlinearity and plasticity is needed. In addition, the geogrid exhibited different stiffness and strength responses in the MD and XMD, which implies that the geogrid's homogenized characteristics is directional dependent (anisotropic). The experimental results, however, indicated that the degree of anisotropy in both the elastic ($E_{XMD}/E_{MD} = 1.35$) and the plastic ($\sigma_{XMD}/\sigma_{MD} = 1.6$) regimes is small, and therefore the anisotropy of the biaxial geogrid is not explicitly considered in this study. Alternatively, an average stress–strain relationship that represents an isotropic state between the MD and the XMD responses is adopted to simplify the numerical analysis.

A constitutive model that is capable of simulating the nonlinear elastoplastic material with isotropic hardening is built using ABAQUS software package. The method used to combine the above model features is based on the conversion of the measured strains and stresses into the appropriate input parameters for the software. This is achieved by decomposing the total strain values into elastic and plastic strains to cover the entire range of the geogrid response. The different model components include: (i) The elasticity component is described by an elastic isotropic model where the total stress and the total strain are related using the elasticity matrix; (ii) The plasticity is modeled using von Mises yield criterion with isotropic hardening and associated flow rule; (iii) The isotropic yielding is defined by expressing the uniaxial yield stress as a function of the equivalent uniaxial plastic strain; (iv)The isotropic hardening rule is expressed in ABAQUS using a tabular data of yield stress as function of plastic strains.

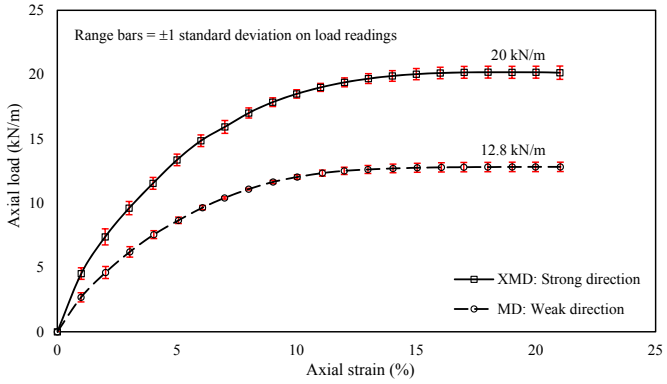

Fig. 2. Experimental axial load-axial strain results in the MD and XMD.

The plasticity data has to be specified in terms of true stresses and true strains (ABAQUS, 2013) despite the fact that test data provides nominal (engineering) values of total stresses and total strains. A procedure is, therefore, needed to convert the nominal test data to its true values and then decompose the total strain values into elastic and plastic strain components to allow for direct data input into ABAQUS. A flow chart that illustrates the procedure adopted to determine the numerical input data based on the experimental results is given in Fig. 3 and summarized in the following steps:

(1) Converting the test data (stresses and strains) from nominal to true values using the following expressions:

$$\varepsilon_{true} = \ln(1 + \varepsilon_{nom}) \quad (1)$$

$$\sigma_{true} = \sigma_{nom}(1 + \varepsilon_{nom}) \quad (2)$$

Where: ε_{true} is the true strain, ε_{nom} is the nominal strain, σ_{true} is the true stress, and ε_{nom} is the nominal stress.

Then, decompose the total true strain (ε_{true}) into elastic and plastic components (Fig. 4a):

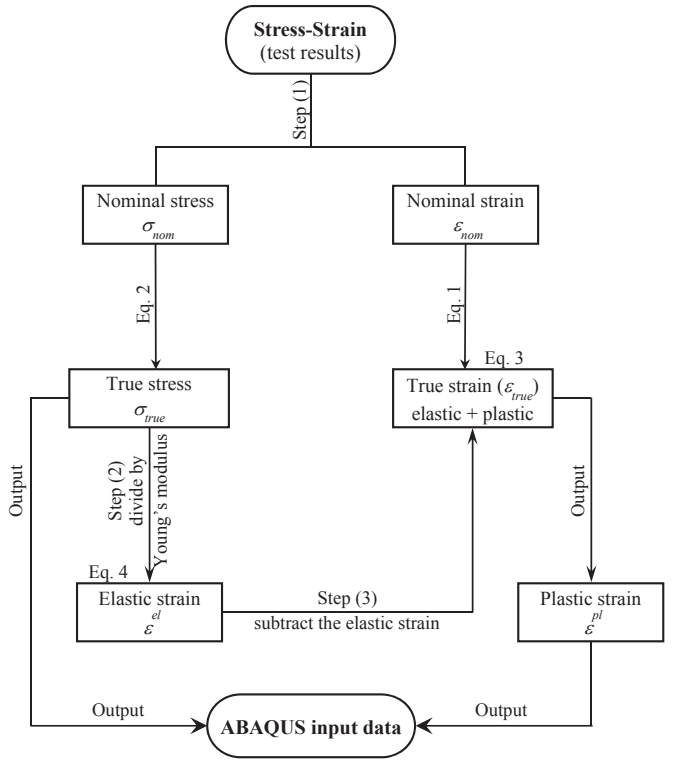

Fig. 3. Procedure used to generate ABAQUS input parameters.

$$\varepsilon_{\text{true}} = \varepsilon^{el} + \varepsilon^{pl} \tag{3}$$

Where: ε^{el} is the elastic strain and ε^{pl} is the plastic strain.

(2) Using the true stress (σ_{true}) and Young's modulus (E) to obtain the elastic strain component (ε^{el}):

$$\varepsilon^{el} = \sigma_{true}/E \tag{4}$$

(3) Subtract the elastic strain value from the total true strain to obtain the plastic strain.

The final geogrid plasticity properties are introduced into ABAQUS input module in terms of true stresses versus plastic strains.

The elastic–plastic model described above assumes that the material behavior is linear elastic at small strain levels with a relatively small elastic limit compared to the ultimate strength of the material. The elasticity is characterized by Young's modulus and Poisson's ratio and is immediately followed by a nonlinear response due to the development of large plastic deformation (Dean and Mera, 2004). Due to the fact that the elastic limit is very small, the geogrid elasticity model is described using initial tangent modulus that was calculated to be 605 MPa. A Poisson's ratio of 0.3 was used for the geogrid material, as suggested by Liu et al. (2007) and Kwon et al. (2008). The hardening rule data used to describe the geogrid plasticity model is shown in Fig. 4b.

The von Mises yield criterion is known to provide a scalar measure of stress and strain that can generalize the 1D stress state (uniaxial test observations) into 3D state with six components. It is generally assumed that for a given stress state, there exists an equivalent uniaxial (von Mises) stress state and the material yields when the equivalent stress becomes equals to the yield stress:

$$\sigma_e = \sigma_y \tag{5}$$

Where: σ_e is equivalent (von Mises) stress and σ_y is the one-dimensional yield stress from the uniaxial tensile test.

The equivalent stress can be written in terms of principal stresses as follows:

$$\sigma_e = \sqrt{3J_2} = \left\{\frac{1}{2}\left[(\sigma_1-\sigma_2)^2 + (\sigma_2-\sigma_3)^2 + (\sigma_3-\sigma_1)^2\right]\right\}^{\frac{1}{2}} \tag{6}$$

Where J_2 is the second invariant of the deviatoric stress expressed as:

$$J_2 = \frac{1}{6}\left\{(\sigma_1-\sigma_2)^2 + (\sigma_2-\sigma_3)^2 + (\sigma_3-\sigma_1)^2\right\} \tag{7}$$

Using the equivalent stress, the yield function can be defined as:

$$f'(\sigma) = \sigma_e^2 - \sigma_y^2 = 3J_2 - \sigma_y^2 = 0 \tag{8}$$

The counterpart of the equivalent stress is the von Mises effective strain (ε_e) that can be obtained by integrating the equivalent strain increment as:

$$\varepsilon_e = \int d\varepsilon_e \tag{9}$$

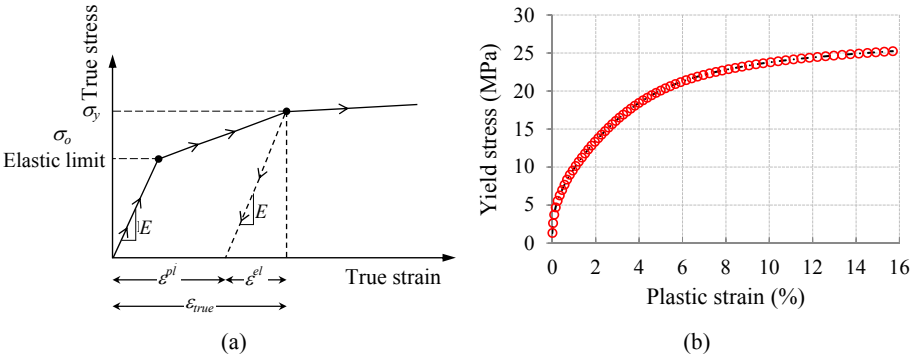

Fig. 4. Geogrid plasticity model: a) decomposition of the total true strain (ABAQUS, 2013), b) hardening rule.

Where $d\varepsilon_e$ is the strain increment that can be determined using:

$$d\varepsilon_e = \left\{\frac{2}{9}\left[(d\varepsilon_1 - d\varepsilon_2)^2 + (d\varepsilon_2 - d\varepsilon_3)^2 + (d\varepsilon_3 - d\varepsilon_1)^2\right]\right\}^{\frac{1}{2}} \quad (10)$$

It should be noted that the scalar plastic strain (ε^{pl}) in one-dimensional plasticity (illustrated in Fig. 3) becomes a tensor in multidimensional plasticity analysis.

Although the above material model allows for the geogrid behavior to be closely represented, it does not consider cyclic loading or creep behavior of the polymeric material. In addition, the loading rate used in the numerical analysis is limited to that used in the experiment.

Geometry and boundary conditions: The biaxial geogrid used in this study consists of three main elements: longitudinal ribs, transverse bars and connecting junctions. These elements are combined together to form the geogrid's network structure. The details of the true geometry (Fig. 1) are explicitly simulated considering the thicknesses of different elements and the aperture structure. To model the uniaxial tensile test, in the longitudinal (X–X) direction the geogrid is restrained along the right side ($U_x = 0$) and the load is applied from the opposite side using a prescribed velocity (V_x) with constant strain rate similar to that used in the experiments (10% strain/min). The geogrid movements are constrained in the transverse direction (Y–Y) at both ends to simulate the friction between the MTS grips and the geogrid. This loading procedure was used consistently for all analyzed geogrid models. A numerical simulation is also performed using double-sided loading to examine the difference in geogrid response compared to single-side loading. The observed difference was related to the symmetry of the stress and strain distributions, however, the overall stress-strain behavior of the geogrid remains unchanged.

2.2.2. Sensitivity analysis

The purpose of this section is to examine the effect of different numerical factors typically used in finite element analysis on the calculated geogrid response using the proposed numerical model. The investigated factors include the choice of membrane vs. solid elements (element type) and the role of finite element configuration (element shape, size, and interpolation function). Recommendations are then given, in Section 3.2, for the optimal numerical configuration for use in modeling unconfined and soil-confined geogrid.

Membrane (triangular and quadrilateral) elements and solid (tetrahedron and hexahedron) elements are first examined. The reason to investigate the response of both types is that membrane elements are typically used to represent thin surfaces that offer in-plane strength but have no bending stiffness (typical response of unconfined geogrid under tensile loading condition), whereas, solid elements are used when the thickness of the structure affects the overall response (in soil, the geogrid thickness contributes toward the bearing resistance component). Both types of elements are used to model the biaxial geogrid using implicit static solver in ABAQUS/Standard. An out-of-plane thickness of 0.8 mm is assigned for membrane elements for both the longitudinal ribs and the transverse bars while the junctions were given a thickness of 2.9 mm. These thicknesses reflect the measured values for the investigated biaxial geogrid (see Fig. 1). Fig. 5 shows a *sample* of the 3D FE mesh using solid elements.

The results showed that no significant difference in response has been calculated and the two elements were found to be able to capture the unconfined geogrid response in both the axial and lateral directions.

The effect of element shape, size, and interpolation function on the response of unconfined geogrid is also examined and showed insignificant effect.

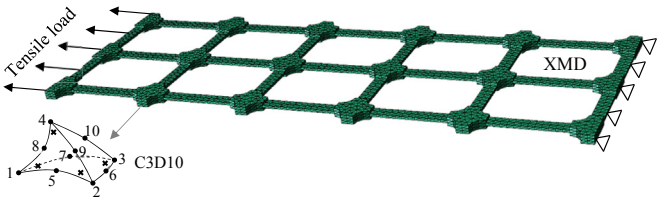

Fig. 5. Sample of the geogrid mesh in three-dimensions.

Several mesh sizes were tested in this section and reference points were used to evaluate the effect on the geogrid response for both membrane and solid elements. The element size was found to have no significant effect on the geogrid response under uniaxial loading when *membrane elements* are used in the analysis. The choice of a mesh size for the geogrid model using *continuum elements* is governed by the geogrid thickness. This is attributed to the fact that the geogrid thickness is significantly small compared to the width of the member. The effect of the mesh size is evaluated using various element sizes from 0.5 t and up to 10 t (where t is the geogrid rib thickness). The results showed that using geogrid mesh with a global average size of 3 t is a reasonable choice as it provides a balance between the stress resolution and the computing time.

2.2.3. Model validation

To validate the proposed FE model for unconfined geogrid, the geogrid specimen is numerically simulated using 8-node continuum brick elements (C3D8).

The calculated and measured (axial) load–strain relationships are compared in Fig. 6. Two reference points located on the longitudinal ribs are used to illustrate the geogrid response: point (I) located near the applied load where necking (maximum lateral strain) was observed in the experiment; point (II) located near the middle of the specimen. A maximum tensile load of 16.5 kN/m, that denotes the strength of the material, was reached at about 15% strain. Beyond the peak load, where necking begins at point (I), the two reference points perform differently. After necking has occurred, all further deformation was found to develop at the neck location, and as a result, point (I) experienced significant strain with a slow rate of decrease in tensile load. Due to the excessive deformation that took place at the neck location, the tensile load is released at other locations within the specimen leading to the unloading observed at point (II). It is worth noting that the calculated response at point (I) is consistent with the measured trend in the experiment.

The numerically calculated response shown in Fig. 6 confirms the assumption of isotropic (average) state in the MD and XMD presented in Fig. 2.

2.3. Response to tensile loading

Although the numerical results allow for the geogrid response in both MD and XMD to be investigated, only the results of the XMD is presented in this section to keep the paper size within manageable limits.

2.3.1. Displacement and stresses in the geogrid

The deformed shape and displacement pattern along the geogrid are illustrated in Fig. 7a for an applied boundary displacement (U_x) of 23 mm (onset of necking). The original geogrid geometry is also shown for comparison purpose. Displacements generally decreased with distance from the applied load (left side) and reached zero at the fixed boundary.

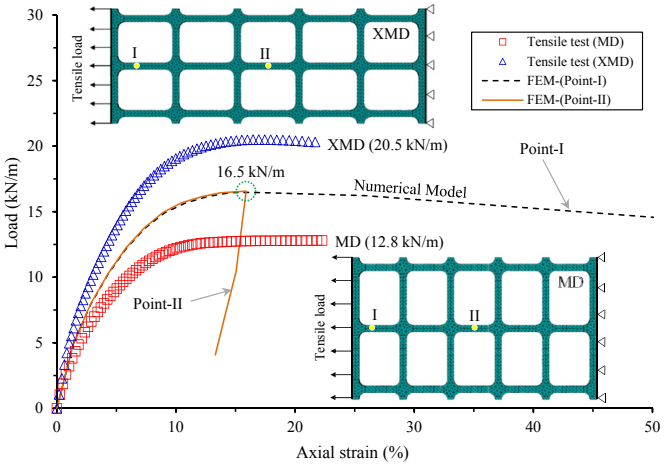

Fig. 6. Model performance: experimental versus calculated results.

The stress distribution within the geogrid is shown in Fig. 7b. In contrast with the displacement pattern, the stresses in the loading direction (S_{xx}) were found to be almost uniform along the longitudinal ribs. Much smaller stress changes were calculated in the transverse bars as well as at the connecting junctions.

Fig. 7c shows the equivalent plastic shear strains (PEEQ) developing in the geogrid under the applied tensile loads. It is evident that plastic strains are concentrated within the necking zone located near the applied load.

The patterns observed in Fig. 7 are confirmed by plotting the normalized displacements along the geogrid as shown in Fig. 8a. Displacement values were found to decrease linearly with distance from the applied load. The stress distribution (Fig. 8b) shows that the longitudinal ribs carry most of the transmitted stresses caused by the applied load with only about one fourth of the stress felt by the junctions. The stress transferred to the transverse bars was found to be negligible.

The total geogrid deformation, in both the axial and lateral directions, is evaluated. The load–displacement response calculated along the loaded geogrid boundary up to the maximum applied load is shown in Fig. 9. The axial displacement, U_x, as the geogrid approaches failure is found to be about 20 mm whereas the lateral displacement, U_y, in the direction normal to the applied load, reached about 0.3 mm before failure.

2.3.2. Axial and lateral strains

Theoretical approaches used in the geosynthetic analysis generally assume uniaxial strain and stress states (Kaliakin and Dechasakulsom, 2001). Experimental evidence, however, indicates that lateral strains manifested in the necking that develops in the longitudinal ribs can significantly affect the geogrid response (Shinoda and Bathurst, 2004). Fig. 10 illustrates the strains calculated in the axial (X) and lateral (Y) directions at three distinct locations. The longitudinal rib (point a) exhibited positive strains (extension) in the axial direction whereas negative strains (contraction) were calculated in the lateral direction (Fig. 10a). In contrast to the longitudinal rib, Fig. 10b shows that transverse bar (point b) experienced extension in the lateral direction while the

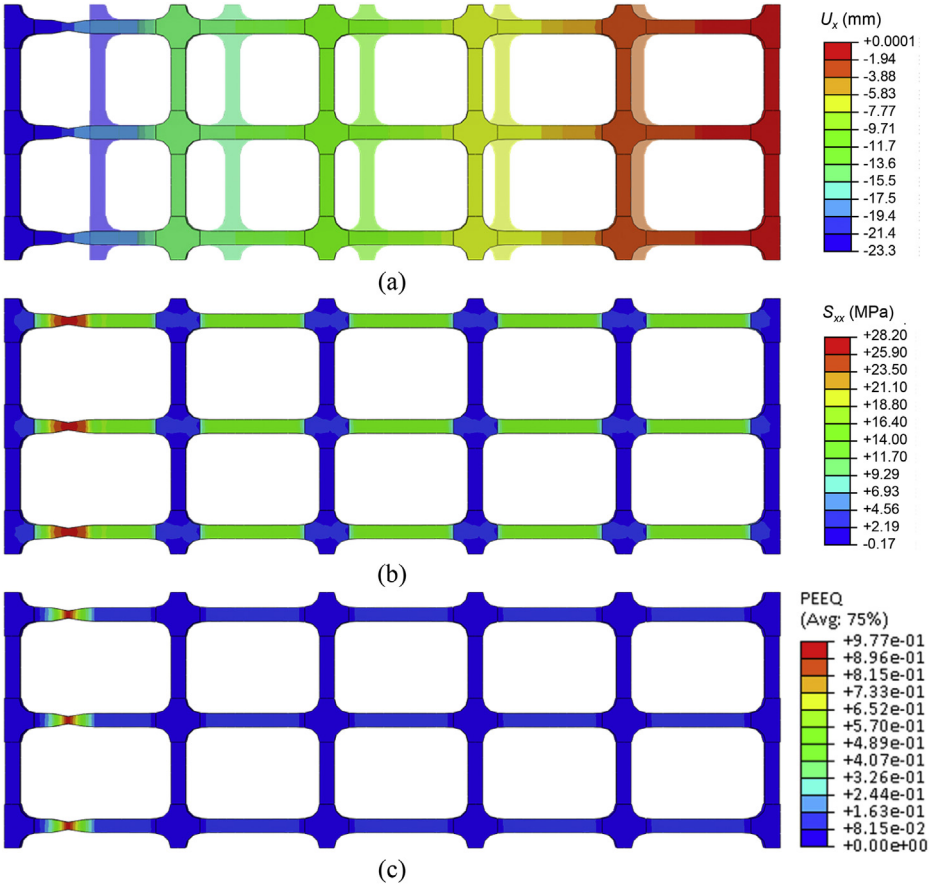

Fig. 7. Geogrid deformation at $U_x = 23$ mm in the XMD: a) displacements (U_x), b) stresses (S_{xx}), c) plastic strains.

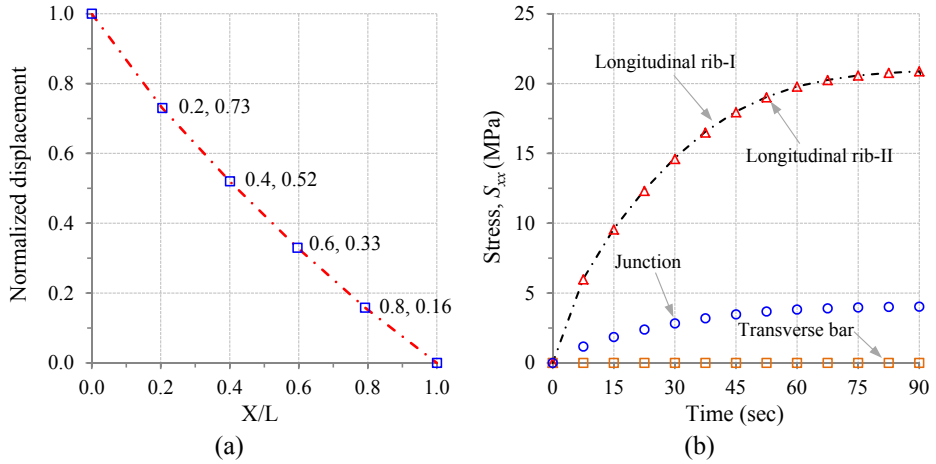

Fig. 8. Geogrid response at applied displacement of 23 mm: a) Displacement distribution with distance (X) from loaded boundary; b) Stress transfer along the geogrid.

axial direction has slightly contracted. The magnitudes of these strains are considered to be insignificant. The junction (point c) exhibited small extension in the loading direction coupled with a smaller contraction in the lateral direction as shown in Fig. 10c.

2.4. Exact geometry vs. planer sheet

Geogrid modeling is conventionally performed using either truss, bar, or cable elements in 2D or equivalent planer sheet in 3D analysis (Yogarajah and Yeo, 1994; Shuwang et al., 1998; Perkins and Edens, 2003; Sugimoto and Alagiyawanna, 2003; El Sawwaf, 2007; Liu et al., 2007; Dong et al., 2011; Mirmoradi and Ehrlich, 2014; El Naggar et al., 2015; Zhuang and Wang, 2015). Modelling geogrid using planer sheet requires extensive calibration to balance the increase in the geometric stiffness.

The biaxial geogrid, used in the current study, involves an open area of around 70% that will bring additional stiffness when the geogrid is modeled as a planer sheet. With the purpose of calibration of the planer sheet to represent the accurate geogrid response, it is necessarily to achieve an equivalent sheet thickness.

To determine an equivalent sheet thickness that produces a similar response to that obtained using the exact geogrid geometry, a numerical model was developed using a planer sheet (62 mm × 189 mm) and the equivalent thickness is then back calculated using the trial and error. The obtained responses are compared with those of the exact geometry as shown in Fig. 11. It is found that using an equivalent thickness of 0.175 mm was able to capture the true behavior of the geogrid. This indicates that modeling the biaxial geogrid as a planer sheet requires a significant thickness reduction as compared to the geogrid rib thickness. This corresponds to about 80% reduction (from 0.8 mm to 0.177 mm) for the biaxial geogrid used in this study.

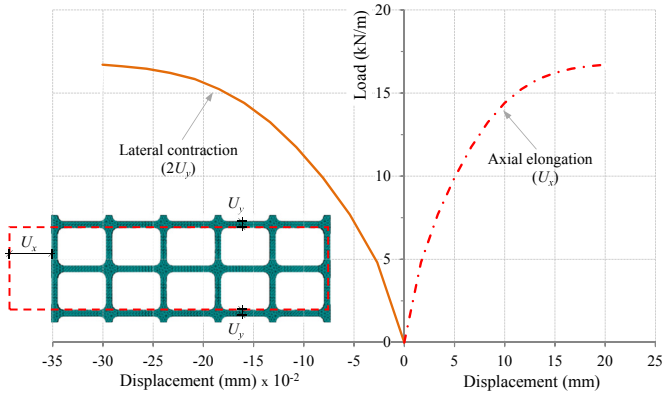

Fig. 9. Total displacements in the axial (U_x) and lateral (U_y) directions.

3. Soil-confined geogrid

The purpose of this section is to examine the applicability of the proposed 3D unconfined geogrid model developed in phase one in modeling soil-geogrid interaction problems. A numerical example involving a square footing over geogrid-reinforced soil is presented.

3.1. Geogrid-reinforced foundation

Bearing capacity of reinforced soils has been studied experimentally by many researches (e.g. Guido et al., 1986; Huang and Tatsuoka, 1990; Das et al., 1994; Adams and Collin, 1997; Dash et al., 2001; Patra et al., 2006; Abu-Farsakh et al., 2008; Tafreshi and Dawson, 2010). These studies demonstrated that the overall effects of using geosynthetic material in increasing the bearing capacity of shallow foundations. The roles of different parameters such as reinforcement length, spacing between reinforcing layers, depth to the upper geosynthetic layer, number of layers, and types of geosynthetics that contribute to the bearing capacity were also investigated in these studies.

Analytical solutions were also developed by researchers (Binquet and Lee, 1975a,b; Huang and Menq, 1997; Kumar and Saran, 2003; Sharma et al., 2009; Chakraborty and Kumar, 2014) to calculate the bearing capacity of reinforced soils.

Numerical analysis is an alternative way to study stresses and strains within a given soil-geosynthetic system. The finite element method has been proven to be effective in the analysis of reinforced foundations problems (Yetimoglu et al., 1994; Kotake et al., 2001; Basudhar et al., 2007; Ghazavi and Lavasan, 2008; Li et al., 2012; Rowe and Liu, 2015). In these studies, modeling geogrid reinforcement was often simplified either using truss elements (in 2D analysis) or a continuous sheet (in 3D analysis). In addition, the interaction between the simplified 3D geogrid models and the surrounding soil was often captured using interface layers in which the contact properties were considered while the interlocking effect was not represented. It is known that soil-geogrid interlocking plays an important role in the load-carrying capacity of foundations

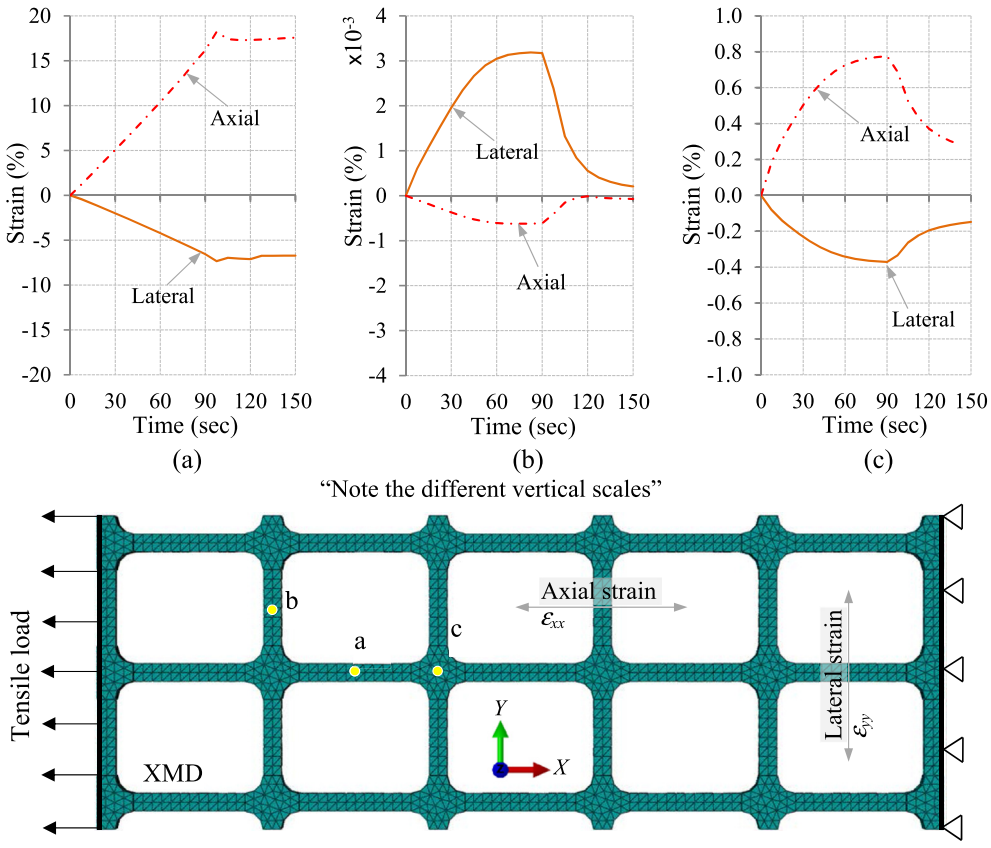

Fig. 10. Axial and lateral strains at different locations along the geogrid: a) longitudinal rib; b) transverse bar; c) junction.

over geogrid-reinforced soils (Guido et al., 1986; Liu, 2015; Pinho-Lopes et al., 2015). The interlocking of soil particles through the grid apertures mobilizes the tensile strength in the reinforcing layer and generates an anchoring effect that leads to better geotechnical performance. Modeling such interactions considering the explicit geogrid geometry has been reported by Tran et al. (2013b) using the finite-discrete element method. The modeling approach presented in phase one of this study is used to simulate a geogrid-reinforced soil supporting a square footing. Using the exact geometry of geogrid allows for the interlocking effect to be explicitly simulated. The soil-geogrid interaction is ensured in this study using interface elements.

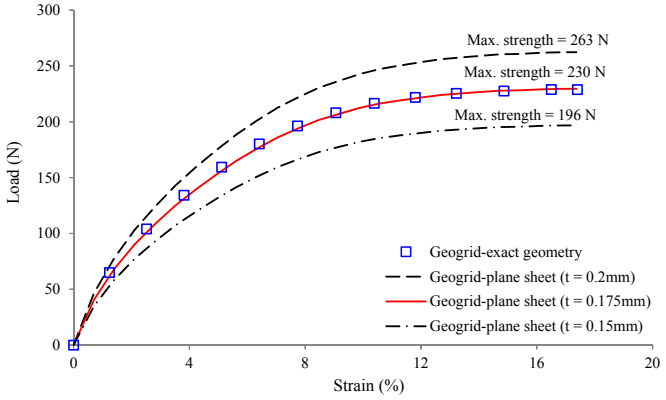

Fig. 11. Effect of modeling geogrid as a planer sheet.

3.2. Numerical modeling of a square footing on geogrid-reinforced soil

The experimental results reported by Chen et al. (2009) for square footing supported by geogrid-reinforced crushed limestone is used to validate the proposed geogrid model. The experiments investigated the effect of introducing geogrid reinforcement on the stress distribution in the soil mass and the strains developing in the geogrid. The model footing was 1 in. (2.54 cm) thick steel plate with dimensions of 6 in. (15.2 cm) × 6 in. (15.2 cm) placed at the center of a rigid container (1.5 m × 0.91 m × 0.91 m). The soil used in the experiment was Kentucky crushed limestone with $D_{50} = 5.66$ mm, maximum dry unit weight of 22.68 kN/m^3, and a peak friction angle of 53°. The elastic modulus of the crushed limestone was estimated from triaxial tests to be 120 MPa. Biaxial geogrids used in this experiments are similar to that used in phase one of this study (Table 1) with dimensions of 1.5 m in length and 0.9 m in width were used in the experiments. The upper geogrid layer was installed at a depth of 50 mm below the foundation base. The number of geogrid layers was varied keeping a distance of 50 mm between two adjacent layers. The vertical stress distribution in the soil was measured using earth pressure cells (10 cm in diameter) installed within the soil mass. The strain distribution in the geogrid reinforcement was measured using strain gauges placed at different locations along the reinforcements.

3.2.1. Details of the numerical model

The 3D finite element models have been developed to simulate the geometry and test procedure used in the experiments. The analysis is performed for up to two geogrid layers using ABAQUS

software package. The exact geogrid geometry (16 longitudinal elements and 21 transverse elements) was modeled using 8-node linear brick elements with eight integration points (Fig. 12). To simplify the nonlinear contact analysis in this case, the local increase in thickness of the junction is not modeled in the analysis. This approximation is expected to cause a slight reduction in the bearing resistance that would develop at these particular locations on the transverse bars.

The geogrid material model developed in phase one of this study is used throughout this analysis. The geogrid is simulated using over 15,300 finite elements as shown in Fig. 12. Only one-quarter of the geometry has been modeled to take advantage of the problem symmetry as illustrated in Figs. 12 and 13.

The crushed stone backfill was modeled using elasto-plastic Mohr-Coulomb failure criteria with non-associated flow rule and the soil domain was discretized using 8-node linear brick elements (C3D8). The input parameters used in the finite element analysis are summarized in Table 2.

Although the unconfined geogrid analysis showed no difference in the behavior of membrane and continuum elements, it was found that modeling soil-geogrid interaction using solid elements is more appropriate as it allows the contact surfaces to be fully defined as compared to the edge-to-edge contact developing when membrane elements are used.

The choice between hexahedral and tetrahedral elements was also governed by the geogrid thickness. Using tetrahedral elements can result in poor aspect ratio, whereas hexahedral elements (e.g. C3D8) are found to be suitable for modeling contact problems involving with elasto-plastic material as it allows for strain discontinuities to be captured. The backfill was divided into three layers as shown in Fig. 13. The bottom soil layer ($Soil_{BOT}$) was first generated in eight stages (10 cm each) and the geostatic stress state was established for each stage. The lower geogrid layer ($Grid_{LOWER}$) and the soil elements needed to fill the openings ($Soil_{OPN}$, with $t_{geogrid}$ 0.8 mm) are introduced in a separate step. A second soil layer ($Soil_{MID}$) of 5 cm in thickness was then added. Similarly, the upper geogrid layer ($Grid_{UPPER}$) with soil elements inside the openings was added. Finally, the third soil layer ($Soil_{TOP}$) of 5 cm in thickness was generated up to the soil surface.

Full interlocking between the soil and the geogrid is assumed and therefore, the soil-geogrid interaction was simulated using two fully bonded master/slave contact surfaces. This will prevent slippage from happening at the soil-geogrid interface. The surface based constraints are enforced by eliminating the degrees of freedom of the slave surface to maintain the same transitional and rotational motion equal to those of the master surface. This has been achieved by assigning the soil as the master surface and the geogrid as the slave surface.

Boundary conditions were defined such that the nodes along the vertical boundaries may only translate freely in the vertical direction (smooth rigid). Nodes at the base are fixed against displacements in all directions (rough rigid). Symmetry boundary conditions were assigned at the centerlines as illustrated in Figs. 12 and 13.

Sensitivity analysis was conducted using different element sizes to determine a suitable mesh reinforcement that brings a balance between accuracy and computing time. The 3D FE mesh, with over 112,875 elements, is shown in Fig. 13a. The mesh size was adjusted in the vertical direction around the geogrid layers to provide sufficient resolution within the interaction area. The mesh was also refined in both *X* and *Y* directions around the areas where stress concentration is expected as a result of the footing pressure. A partial view of soil-geogrid interaction is shown in Fig. 13b. It is worth noting that soil elements located above and below the geogrid can interact directly with each other leading to soil continuity through the openings which closely simulates the real behavior of soil-geogrid interaction. Fig. 14 shows further modeling details of the soil-geogrid interaction with emphasize on the soil within the geogrid apertures. In doing so, the model incorporates three interface conditions: i) soil-to-soil; ii) soil-to-geogrid on horizontal surfaces; iii) soil-to-geogrid on vertical surfaces within the geogrid apertures.

After the FE model was built, the square rigid footing was simulated and the surface pressure was applied in small increments

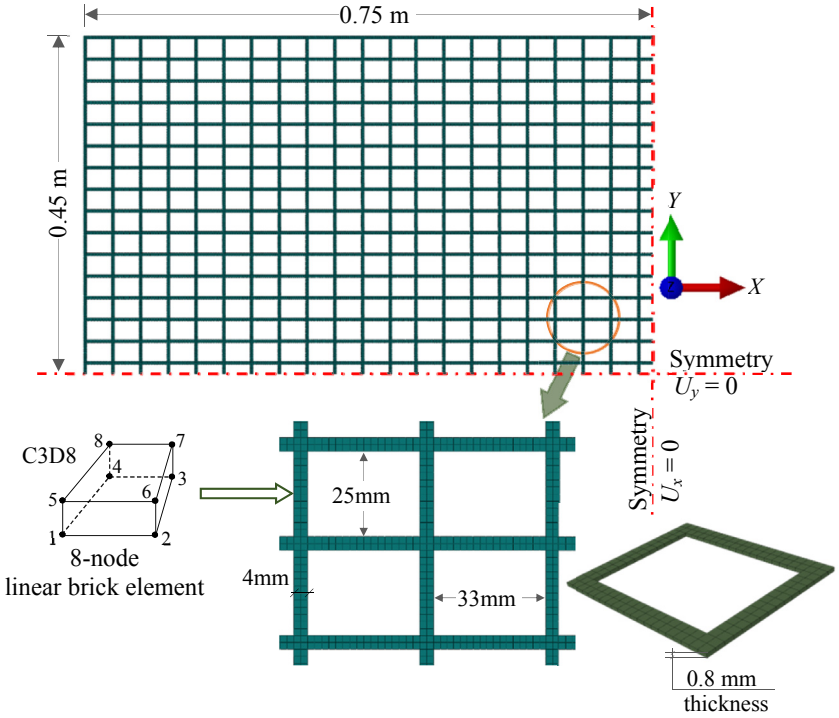

Fig. 12. Plan view of the geogrid mesh for the in-soil model.

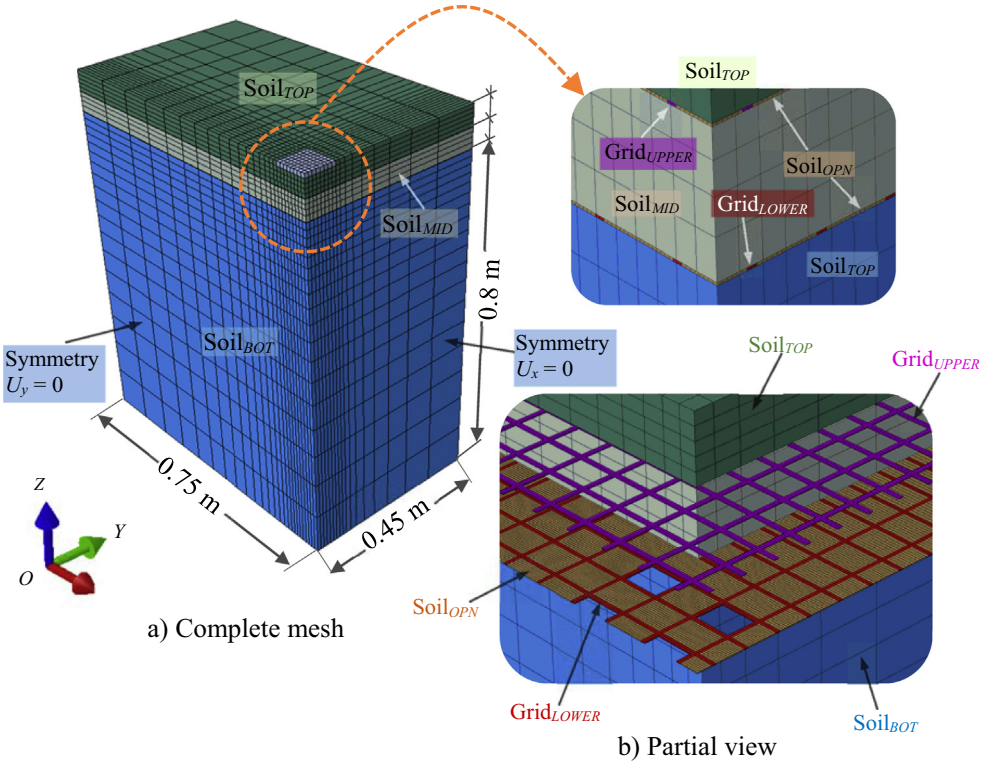

Fig. 13. Complete and partial 3D mesh geometry of the in-soil FE model.

Table 2
Soil input parameters used in the FE analysis.

Elastic Modulus, E (MPa)	Poisson's ratio ν	Friction angle[a] $\phi°/\phi_{cv}°$	Dilatancy angle[b] $\psi°$	Cohesion (MPa)
120	0.35	53/36	21	1E-05

[a] $\phi°$ = peak friction angle & $\phi_{cv}°$ = critical state friction angle.
[b] Determined using Bolton's equation (1986).

using displacement control. For each load increment, the applied pressure was kept constant until the convergence condition was satisfied. The equivalent footing pressure is computed as the summation of the vertical reaction forces divided by the footing area.

3.2.2. Validation of the in-soil model

In this section, the effect of introducing one or two geogrid reinforcement layers into the backfill material is examined and compared with the unreinforced case. To validate the proposed model, the FE results are compared with the experimental data. Fig. 15 shows the relationship between the equivalent footing pressure and the vertical settlement for the three investigated cases: no reinforcement ($N = 0$), one geogrid layer ($N = 1$), and two geogrid layers ($N = 2$). The load-carrying capacity generally increased when geogrid reinforcement was introduced and the ultimate bearing capacity of the footing increased with the addition of a second geogrid layer. The load-settlement results obtained using the developed numerical model agreed reasonably well with

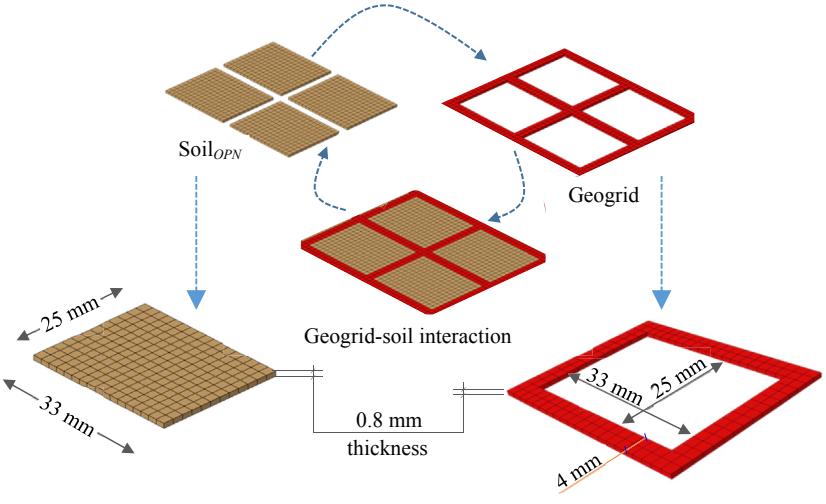

Fig. 14. Details of geogrid-soil interaction.

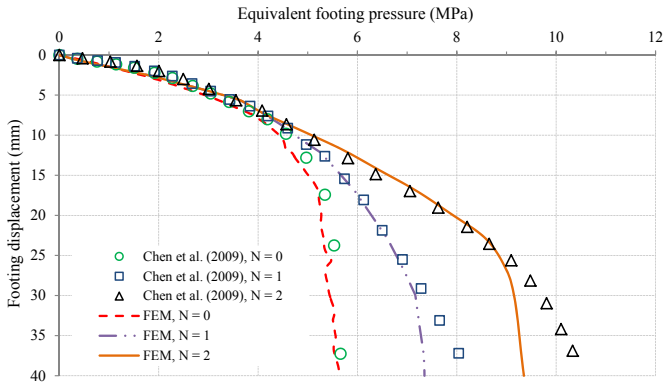

Fig. 15. Load-settlement relationships for geogrid-reinforced crushed limestone.

the experiment data reported by Chen et al. (2009) up to a footing displacement of about 25 mm. As failure is approached for the reinforced cases, the model slightly underestimated the bearing capacity of the footing.

3.3. Response of the geogrid

The deformed shapes of the geogrid layers for a given footing pressure are shown in Fig. 16. A reference pressure value of 6 MPa (smaller than the ultimate capacity for $N = 1$) was chosen to allows for the displacements of the reinforced foundation to be examined. The vertical displacements developing in the geogrid for the reinforced cases are shown in Fig. 16. The maximum displacement was found to decrease with the addition of a second geogrid layer. For $N = 2$ (Fig. 16b), the vertical displacement of the upper layer (located closer to the footing) is larger than that of the lower one. Similarly, the tensile stresses, S_{xx} and S_{yy}, developing in the geogrid decreased when two geogrid layers were installed under the footing, as shown in Fig. 17, with the upper geogrid layer carrying more tensile stresses compared to the lower layer. In both cases, most of the geogrid deformations and stresses occurred mainly in the area immediately below the footing with very small deformation away from the loaded area.

The above example demonstrates that the proposed approach for modeling unconfined geogrid in 3D is suitable for solving geogrid-reinforced soil systems. The results showed that the model can capture the essential interlocking and friction mechanisms that allow for the response of these systems to be evaluated.

4. Summary and conclusions

In this study, a procedure for the 3D finite element analysis of unconfined and soil-confined geogrid is developed using ABAQUS software. A numerical model that is capable of simulating the response of the unconfined biaxial geogrid under tensile loading is first introduced and validated using index test results. In

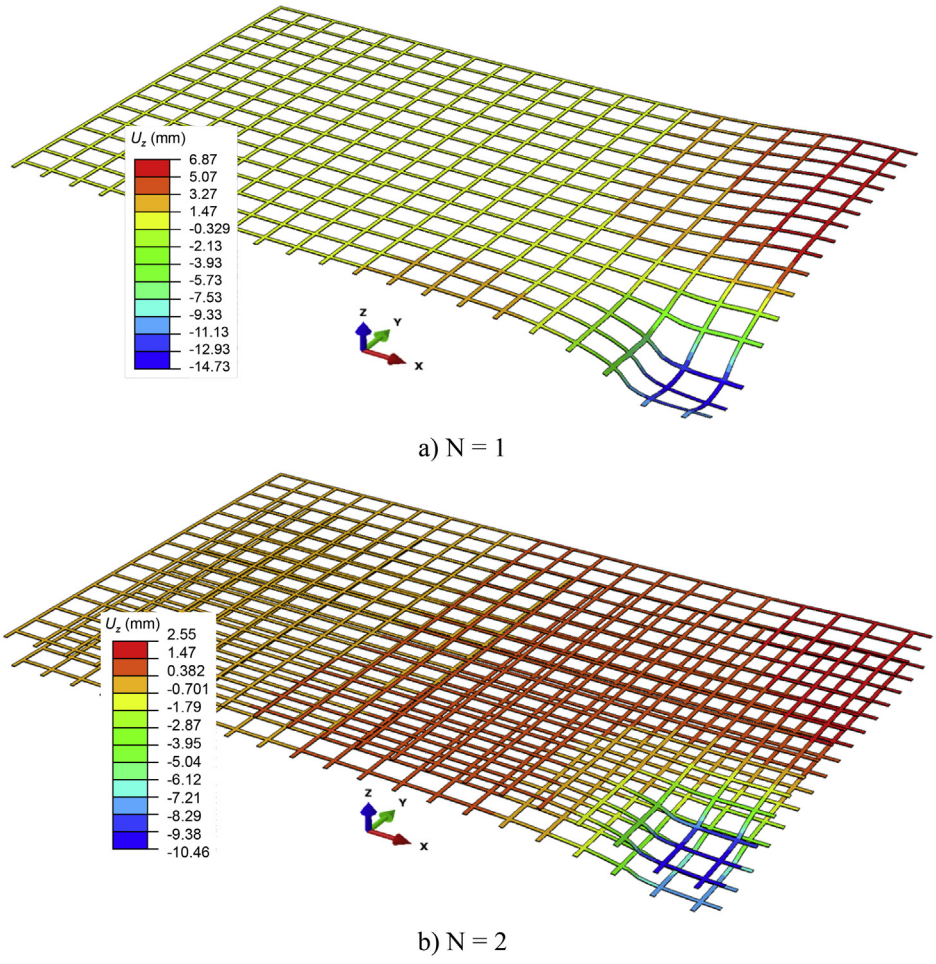

Fig. 16. Geogrid deformation at a given footing load (6 MPa): a) one layer of geogrid; b) two layers of geogrid.

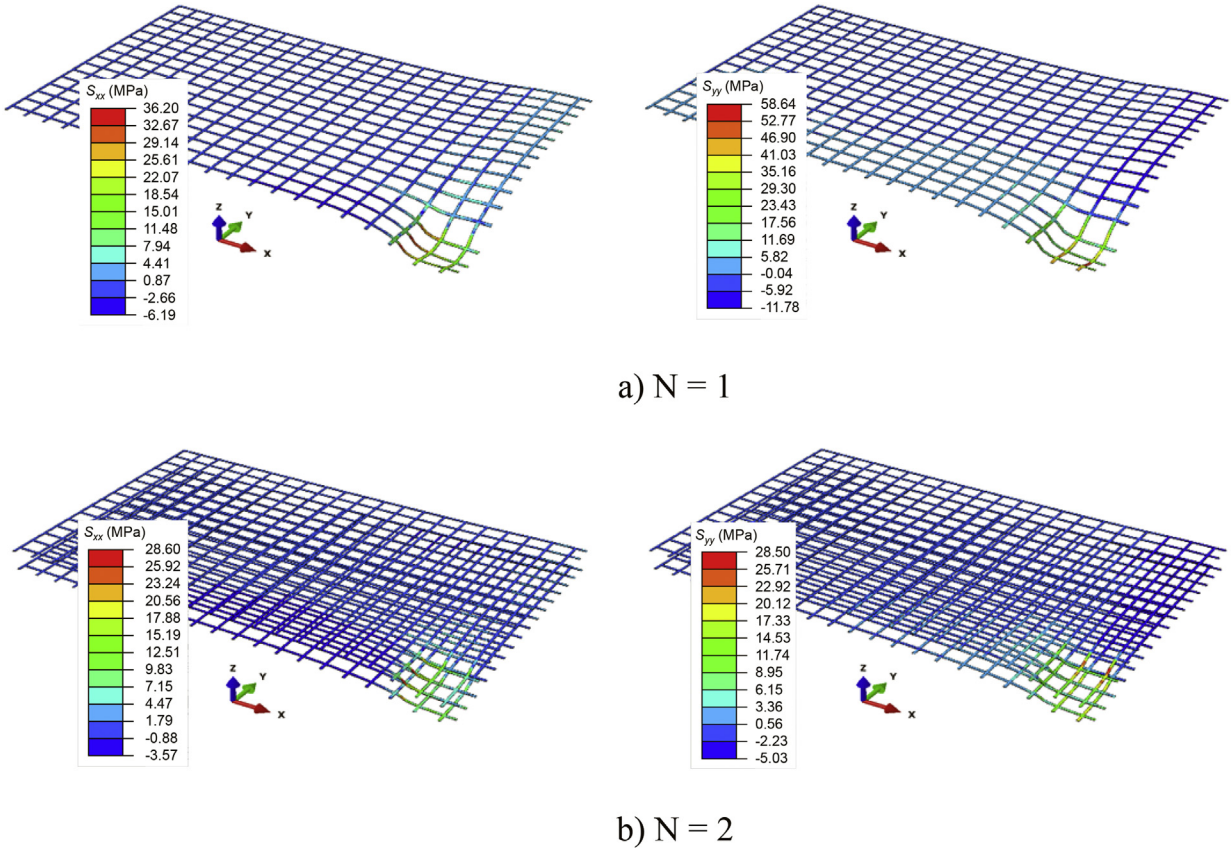

Fig. 17. Tensile stresses (S_{xx} & S_{yy}) at footing pressure of 6 MPa: a) one layer of geogrid; b) two layers of geogrid.

developing this model, the details of the geometrical features are explicitly simulated. Sensitivity analysis was performed to evaluate the role of different numerical parameters on the predicted geogrid response. The difference between modelling the exact geogrid geometry as opposed to an equivalent sheet is also examined.

Tensile load applied to a geogrid specimen causes stresses that are carried mostly by the longitudinal ribs in the direction of the applied load and the portion transmitted to the junctions and transverse bars are insignificant. The displacement is found to decrease linearly with distance from the loaded boundary. Using equivalent plane sheet without proper calibration with exact geometry to model geogrid may lead to a much stiffer response resulting in an overestimation in the design load.

To confirm the validity of the unconfined geogrid model, a 3D analysis is conducted to investigate the geogrid performance as it interacts with the backfill material. A case study involving a square footing supported by a geogrid-reinforced material is investigated. The 3D geometry of the geogrid, its deformation, and stress distribution were presented. The model was able to capture the 3D response of the soil-geogrid system with one or more geogrid layers installed under the footing. Increasing the number of geogrid layers resulted in an increase in the ultimate bearing capacity of the system. The geogrid deformations and tensile stresses for the case of $N = 1$ were found to be generally larger than those calculated for $N = 2$.

Finally, the proposed FE approach has proven to be efficient in capturing the 3D responses of both unconfined and soil-confined geogrid and can be adopted by researchers for soil-geogrid interaction analysis.

Acknowledgements

This research is supported by the Natural Sciences and Engineering Research Council of Canada (NSERC) under grant number 311971-11.

References

ABAQUS, 2013. ABAQUS User's Manuals, Version 6.13. Dassault Systems Simulia Corp., Providence, RI, USA.
Abdi, M.R., Zandieh, A.R., 2014. Experimental and numerical analysis of large scale pull out tests conducted on clays reinforced with geogrids encapsulated with coarse material. Geotext. Geomembr. 42, 494–504.
Abu-Farsakh, M.Y., Chen, Q., Yoon, S., 2008. Use of Reinforced Soil Foundation (RSF) to Support Shallow Foundation. Final Report. Louisiana Transportation Research Center (LTRC), Louisiana Department of Transportation and Development, Baton Rouge, LA, p. 195. Report No. FHWA/LA.07/424.
Adams, M.T., Collin, J.G., 1997. Large model spread footing load tests on geosynthetic reinforced soil foundations. J. Geotech. Geoenviron. Eng. 123, 66–72.
ASTM-D6637-11, 2011. Standard Test Method for Determining Tensile Properties of Geogrids by the Single or Multi-rib Tensile Method, vol. 04.09. ASTM International, Book of ASTM Standards, West Conshohocken, PA, USA.
Basudhar, P.K., Saha, S., Deb, K., 2007. Circular footings resting on geotextile-reinforced sand bed. Geotext. Geomembr. 25, 377–384.
Bathurst, R.J., Kaliakin, V.N., 2005. Review of numerical models for geosynthetics in reinforcement applications. In: 11th International Conference of the International Association for Computer Methods and Advances in Geomechanics, Torino, Italy, pp. 407–416.
Binquet, J., Lee, K.L., 1975a. Bearing capacity analysis of reinforced earth slabs. J. Geotech. Eng. Div. 101, 1257–1276.
Binquet, J., Lee, K.L., 1975b. Bearing capacity tests on reinforced earth slabs. J. Geotech. Eng. Div. 101, 1241–1255.
Bolton, M.D., 1986. The strength and dilatancy of sands. Géotechnique 65–78.
Chakraborty, D., Kumar, J., 2014. Bearing capacity of strip foundations in reinforced soils. Int. J. Geomech. 14, 45–58.

Chen, Q., Abu-Farsakh, M., Sharma, R., 2009. Experimental and analytical studies of reinforced crushed limestone. Geotext. Geomembr. 27, 357–367.
Das, B.M., Shin, E.C., Omar, M.T., 1994. The bearing capacity of surface strip foundations on geogrid-reinforced sand and clay — a comparative study. Geotech. Geol. Eng. 12, 1–14.
Dash, S.K., Krishnaswamy, N.R., Rajagopal, K., 2001. Bearing capacity of strip footings supported on geocell-reinforced sand. Geotext. Geomembr. 19, 235–256.
Dean, G., Mera, R., 2004. Determination of Material Properties and Parameters Required for the Simulation of Impact Performance of Plastics Using Finite Element Analysis. National Physical Laboratory (NPL), Middlesex, UK, p. 49. Report No. DEPC-MPR 007.
Dong, Y.-L., Han, J., Bai, X.-H., 2011. Numerical analysis of tensile behavior of geogrids with rectangular and triangular apertures. Geotext. Geomembr. 29, 83–91.
El Naggar, H., Turan, A., Valsangkar, A., 2015. Earth pressure reduction system using geogrid-reinforced platform bridging for buried utilities. J. Geotech. Geoenviron. Eng. 141 (6), 04015024.
El Sawwaf, M.A., 2007. Behavior of strip footing on geogrid-reinforced sand over a soft clay slope. Geotext. Geomembr. 25, 50–60.
Ezzein, F.M., Bathurst, R.J., Kongkitkul, W., 2015. Nonlinear load–strain modeling of polypropylene geogrids during constant rate-of-strain loading. Polym. Eng. Sci. 55 (7), 1617–1627.
Ghazavi, M., Lavasan, A.A., 2008. Interference effect of shallow foundations constructed on sand reinforced with geosynthetics. Geotext. Geomembr. 26, 404–415.
Guido, V.A., Chang, D.K., Sweeney, M.A., 1986. Comparison of geogrid and geotextile reinforced earth slabs. Can. Geotech. J. 23, 435–440.
Huang, C.-C., Tatsuoka, F., 1990. Special issue on geosynthetic reinforcement in foundations bearing capacity of reinforced horizontal sandy ground. Geotext. Geomembr. 9, 51–82.
Huang, C., Menq, F., 1997. Deep-footing and wide-slab effects in reinforced sandy ground. J. Geotech. Geoenviron. Eng. 123, 30–36.
Hussein, M.G., Meguid, M.A., 2013. Three-dimensional finite element analysis of soil-geogrid interaction under pull-out loading condition. In: GeoMontreal, 66th Canadian Geotechnical Conference. Canadian Geotechnical Society, Montreal, Quebec, Canada, pp. 452–458.
Kaliakin, V.N., Dechasakulsom, M., 2001. Time-dependent Behavior of Geosynthetic Reinforcement – a Review of Mathematical Models. Report No. 01-2. Department of Civil and Environmental Engineering, University of Delaware, p. 14.
Kongkitkul, W., Chantachot, T., Tatsuoka, F., 2014. Simulation of geosynthetic load–strain–time behaviour by the non-linear three-component model. Geosynth. Int. 21 (4), 244–255.
Kotake, N., Tatsuoka, F., Tanaka, T., Siddiquee, M.S.A., Huang, C.-C., 2001. FEM simulation of the bearing capacity of level reinforced sand ground subjected to footing load. Geosynth. Int. 501–549.
Kumar, A., Saran, S., 2003. Bearing capacity of rectangular footing on reinforced soil. Geotech. Geol. Eng. 21, 201–224.
Kwon, J., Tutumluer, E., Konietzky, H., 2008. Aggregate base residual stresses affecting geogrid reinforced flexible pavement response. Int. J. Pavement Eng. 9, 275–285.
Li, F.-L., Peng, F.-L., Tan, Y., Kongkitkul, W., Siddiquee, M.S.A., 2012. FE simulation of viscous behavior of geogrid-reinforced sand under laboratory-scale plane-strain-compression testing. Geotext. Geomembr. 31, 72–80.
Liu, H.L., Ng, C.W.W., Fei, K., 2007. Performance of a geogrid-reinforced and pile-supported highway embankment over soft clay: case study. J. Geotech. Geoenviron. Eng. 133, 1483–1493.
Liu, H., 2015. Reinforcement load and compression of reinforced soil mass under surcharge loading. J. Geotech. Geoenviron. Eng. 141 (6), 04015017.
McDowell, G., Harireche, O., Konietzky, H., Brown, S., Thom, N., 2006. Discrete element modelling of geogrid-reinforced aggregates. Proc. ICE-Geotech. Eng. 159, 35–48.
Mirmoradi, S.H., Ehrlich, M., 2014. Numerical evaluation of the behavior of GRS walls with segmental block facing under working stress conditions. J. Geotech. Geoenviron. Eng. 141 (3), 04014109.
Mosallanezhad, M., Taghavi, S.H.S., Hataf, N., Alfaro, M.C., 2016. Experimental and numerical studies of the performance of the new reinforcement system under pull-out conditions. Geotext. Geomembr. 44 (1), 70–80.
Patra, C.R., Das, B.M., Bhoi, M., Shin, E.C., 2006. Eccentrically loaded strip foundation on geogrid-reinforced sand. Geotext. Geomembr. 24, 254–259.
Perkins, S.W., 2000. Constitutive modeling of geosynthetics. Geotext. Geomembr. 18, 273–292.
Perkins, S.W., 2001. Numerical Modeling of Geosynthetic Reinforced Flexible Pavements. Montana Department of Transportation, Helena, Montana, p. 97. Report No. FHWA/MT-01/003/99160–2.
Perkins, S.W., Edens, M.Q., 2003. Finite element modeling of a geosynthetic pullout test. Geotech. Geol. Eng. 21, 357–375.
Pinho-Lopes, M., Paula, A.M., Lopes, M.L., 2015. Pullout response of geogrids after installation. Geosynth. Int. 22 (5), 339–354.
Rowe, R.K., Mylleville, B.L.J., 1994. Analysis and design of reinforced embankments on soft or weak foundations. In: Bull, J.W. (Ed.), Soil-structure Interaction: Numerical Analysis and Modelling. Chapman & Hall, pp. 231–260.
Rowe, R.K., Liu, K.W., 2015. Three-dimensional finite element modelling of a full-scale geosynthetic-reinforced, pile-supported embankment. Can. Geotech. J. 52 (12), 2041–2054.
Sharma, R., Chen, Q., Abu-Farsakh, M., Yoon, S., 2009. Analytical modeling of geogrid reinforced soil foundation. Geotext. Geomembr. 27, 63–72.
Shinoda, M., Bathurst, R.J., 2004. Lateral and axial deformation of PP, HDPE and PET geogrids under tensile load. Geotext. Geomembr. 22, 205–222.
Shuwang, Y., Shouzhong, F., Barr, B., 1998. Finite-element modelling of soil-geogrid interaction dealing with the pullout behaviour of geogrids. Acta Mech. Sin. 14, 371–382.
Sugimoto, M., Alagiyawanna, A., 2003. Pullout behavior of geogrid by test and numerical analysis. J. Geotech. Geoenviron. Eng. 129, 361–371.
Tafreshi, S.N.M., Dawson, A.R., 2010. Behaviour of footings on reinforced sand subjected to repeated loading – comparing use of 3D and planar geotextile. Geotext. Geomembr. 28, 434–447.
Tran, V.D.H., Meguid, M.A., Chouinard, L.E., 2013a. The application of coupled finite-discrete element method in analyzing soil-structure interaction problems. In: 3rd International Conference on Particle-based Methods Fundamentals and Applications, Particles 2013, Stuttgart, pp. 200–211.
Tran, V.D.H., Meguid, M.A., Chouinard, L.E., 2013b. A finite-discrete element framework for the 3D modeling of geogrid-soil interaction under pullout loading conditions. Geotext. Geomembr. 37, 1–9.
Wang, Z., Jacobs, F., Ziegler, M., 2016. Experimental and DEM investigation of geogrid–soil interaction under pullout loads. Geotext. Geomembr. 44 (3), 230–246.
Yetimoglu, T., Wu, J., Saglamer, A., 1994. Bearing capacity of rectangular footings on geogrid-reinforced sand. J. Geotech. Eng. 120, 2083–2099.
Yogarajah, I., Yeo, K.C., 1994. Finite element modelling of pull-out tests with load and strain measurements. Geotext. Geomembr. 13, 43–54.
Zhuang, Y., Wang, K.Y., 2015. Three-dimensional behavior of biaxial geogrid in a piled embankment: numerical investigation. Can. Geotech. J. 52 (10), 1629–1635.